

Spectral Shapes of Pair Annihilation Line Emission in Magnetar Giant Flares

TOMOKI WADA   AND SHIGEO S KIMURA  

¹*Frontier Research Institute for Interdisciplinary Sciences, Tohoku University, Sendai, Japan*

²*Astronomical Institute, Graduate School of Science, Tohoku University, Sendai, Japan*

³*Department of Physics, National Chung Hsing University, Taichung, Taiwan*

ABSTRACT

We investigate the gamma-ray spectrum in the MeV range arising from electron-positron pair annihilation in fireballs associated with magnetar giant flares (MGFs), motivated by the recent observation of a MeV gamma-ray line feature in a bright gamma-ray burst, GRB 221009A. We develop an analytic model of line emission, demonstrating that relativistic beaming results in a broadened, power-law spectral feature with photon index -1 . We then perform Monte Carlo radiative transfer simulations incorporating electron-positron pair production, annihilation, and Compton scattering. The dependence of the emergent spectrum on the baryon loading is also examined, showing that a baryon-poor fireball is more favorable for the detection of MeV gamma rays. We further assess the detectability of the line component. The simulation results indicate that a power-law MeV component from the initial spike of a Galactic MGFs could be observed with current instruments, such as *Fermi*/GBM, and will be well within the reach of upcoming MeV gamma-ray satellites, which are expected to detect $\mathcal{O}(100)$ photons from such events.

1. INTRODUCTION

Fireballs are high-temperature, optically thick, radiation-dominated plasma that emerges in various high-energy astronomical phenomena. They are formed when a large amount of energy is deposited into a compact region, causing the plasma to reach high temperature where electron-positron pair production is ignited. Some of high-energy emission in astronomical transients are thought to originate from these fireballs. Part of the emission associated with gamma-ray bursts (GRBs; e.g., Goodman 1986; Paczynski 1986; Shemi & Piran 1990; Meszaros et al. 1993; Mészáros & Rees 2000; and see Piran 1999; Zhang 2018 for reviews), magnetar giant flares (MGFs; Thompson & Duncan 1995, 2001; Nakar et al. 2005; and see Kaspi & Beloborodov 2017 for reviews), and less energetic, magnetar short bursts (MSBs) are possible examples of those astronomical transients. In the fireballs in MGFs and some of MSBs (Thompson & Duncan 2001; Ioka 2020; Yang & Zhang 2021; Wada & Ioka 2023; Wada & Shimoda 2024; Wada & Asano 2025; Shimoda & Wada 2025), the initially opaque fireball expands and is accelerated up to a relativistic speed, undergoing adiabatic cooling. This cooling reduces the number density of electron-positron pairs in thermal equilibrium, eventually allowing photons to decouple and escape from the plasma. Consequently, the fireball emits high-energy radiation.

GRB 221009A, often referred to as the “Brightest of All Time,” was discovered on October 9, 2022. This is the brightest GRB ever observed so far (An et al. 2023; Frederiks et al. 2023; Kann et al. 2023; Lesage et al. 2023; LHAASO Collaboration et al. 2023; Axelsson et al. 2024; Kong et al. 2024; Ravasio et al. 2024; Zhang et al. 2024a). The associated host galaxy is at redshift $z \sim 0.15$ (Malesani et al. 2023), indicating an isotropic-equivalent luminosity up to $\sim 1.5 \times 10^{55} \text{ erg s}^{-1}$ (An et al. 2023). Partly because of its extreme isotropic-equivalent energy, GRB 221009A has brought new insights regarding GRBs not found so far, such as the observation of the TeV afterglow (LHAASO Collaboration et al. 2023; LST Collaboration et al. 2025), non-detection of neutrino (Murase et al. 2022; Ai & Gao 2023; Abbasi et al. 2023; Veres et al. 2024), and so on (see also e.g., Das & Razzaque 2023; Zhang et al. 2025; Kusafuka & Asano 2025).

One of the remarkable discoveries associated with GRB 221009A is the detection of a mysterious gamma-ray line emission in MeV range. This spectral feature, identified by Ravasio et al. (2024); Zhang et al. (2024a); Burns et al. (2024), was observed between 246 s and 360 s after the trigger time of *Fermi*/GBM. This line exhibits a time-varying central energy, $\varepsilon_{\text{line}}$, from $\sim 37 \text{ MeV}$ to $\sim 6 \text{ MeV}$, with a relatively narrow spectral width of $\Delta\varepsilon \sim 2 \text{ MeV}$. Electron-positron pair annihilation in the jet naturally produces such line emis-

sions in the MeV energy range. This scenario requires high-latitude emission from the GRB jet to explain the observed time evolution (Zhang et al. 2024b; Pe'er & Zhang 2024). Other possible interpretations are also suggested: A line emission from heavy elements (Wei et al. 2024); optical depth discussion (Yi et al. 2024); down-Comptonization (Liu et al. 2025); neutron capture scenario (Zhu et al. 2025). Probable evidence for another MeV line emission has also been reported in GRB 221023A (Jiang et al. 2025). Such a line emission from GRBs had already been studied prior to this observation (Pe'er & Waxman 2004; Pe'er et al. 2006; Ioka et al. 2007; Murase & Ioka 2008).

The detection of the MeV line from a GRB implies that similar line features could be observable in high-energy astrophysical transients beyond GRBs. Line emissions arising from the electron-positron pair annihilation may commonly occur in fireballs of MGFs and MSBs. In particular, MGFs are among the most energetic transient phenomena observed in the Milky Way Galaxy, with three events detected to date (from SGR 0526-66: Evans et al. 1980; from SGR 1900+14: Hurley et al. 1999; Feroci et al. 1999; from SGR 1806-20: Hurley et al. 2005; Mereghetti et al. 2005; Boggs et al. 2007; Frederiks et al. 2007; see also Roberts et al. 2021; Mereghetti et al. 2024 for possible extragalactic MGFs). Motivated by the recent observations of the line emission, we investigate the spectral properties of electron-positron annihilation in MGFs. Using a Monte-Carlo approach, we solve the entire sequence of MeV photons production, propagation, and annihilation, extending previous one-zone (Pe'er & Waxman 2004; Pe'er et al. 2006) and analytic (Ioka et al. 2007; Murase & Ioka 2008) models developed for line emission in GRBs, as well as Monte-Carlo studies for GRBs that omit pair processes (Ito et al. 2013, 2014; Lazzati 2016; Chhotray & Lazzati 2018).

This Letter is organized as follows. In section 2, we present an analytic model of the line emission. In section 3, we present the results of numerical simulations for the line emission in MGFs. Section 4 is devoted to the conclusion and discussion. Details of our model and numerical simulations can be found in the Appendices.

2. ANALYTIC MODEL OF SPECTRAL SHAPE

We analytically derive the observed spectrum of line emission originating from a relativistically expanding fireball. The method for calculating the analytic spectrum based on numerical simulation is introduced. For a line emission from a single relativistically expanding shell, the observed spectrum is transformed into a power-law spectrum with cutoffs as a consequence of the

relativistic Doppler effect. The photon index, defined as $dN/d\varepsilon \propto \varepsilon^{-\gamma}$ where N is the photon number and ε is the photon energy, equals -1 , which is determined solely by the geometrical considerations. These analytic results will be confirmed by the numerical calculation in Section 3.

To proceed with the analytic derivation, we adopt the following model assumptions. We consider a spherically expanding relativistic shell of radius r_{em} with a half-opening angle θ_j , moving with a Lorentz factor Γ_{em} ($\gg 1$). The luminosity distance between the observer and the shell is D_l ($\gg r_{\text{em}}$). In the comoving frame of the shell, the photon distribution function is assumed to be isotropic (see Beloborodov 2011, for the angular distribution of photons around a photospheric radius). For given fireball dynamics (see Appendix B for details), the number of photons originating from pair annihilation is determined around a radius r_{an} , where the pair-annihilation timescale becomes longer than the dynamical timescale. In contrast, the photon spectrum is determined at the radius r_{ph} , where the scattering timescale becomes longer than the dynamical timescale. The former lies inside the latter (see Appendix B). r_{em} lies around r_{an} or r_{ph} , and should be determined numerically.

The analytic spectrum is calculated as follows. For photons isotropically distributed in the comoving frame, the photon distribution function is expressed as $f(\varepsilon'; r_{\text{em}})$, where ε' denotes the photon energy in the comoving frame. Using this distribution function, the observed specific flux is given by (see Appendix A for details)

$$F_\varepsilon = \frac{2\pi}{c^2} \left(\frac{r_{\text{em}}}{D_l} \right)^2 \int_{\mu_j}^1 d\mu \mu \varepsilon^3 f(\varepsilon \Gamma_{\text{em}}(1 - \beta \mu); r_{\text{em}}), \quad (1)$$

where $\beta = (1 - \Gamma_{\text{em}}^{-2})^{1/2}$, μ represents the cosine of the angle between the radial direction and the photon momentum, and μ_j is the cosine at the edge of the emitting shell. For a spherical shell, μ_j equals 0. The photon distribution function at r_{em} is determined by the plasma number density and the pair annihilation rate, which will be calculated numerically using the Monte Carlo method following the procedure of Ramaty & Meszaros (1981). The analytic spectrum is presented in Section 3.

To determine r_{em} , where contributes most significantly to the emission spectrum, detailed numerical simulations incorporating photon production, propagation, and absorption are required. We carried out radiation transfer simulations, including these processes, for the parameters of MGFs (see section 3 for detailed values), and found $r_{\text{em}} = 7.5 \times 10^6$ cm (corresponding to the comoving temperature of $T \simeq 25$ keV, the optical depth

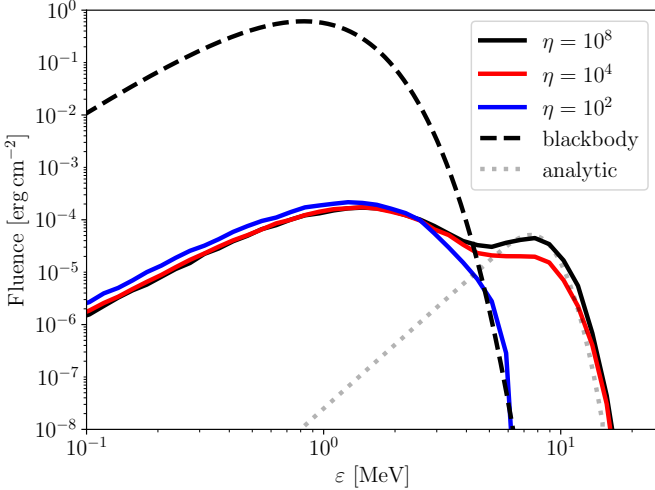


Figure 1. Spectra of the observed line emission from fireballs with different specific enthalpies (solid lines), the primary blackbody radiation (black dashed line), and analytic model derived in Section 2 (gray dotted line). The adopted parameters are shown in Section 3. The spectra originally characterized by Equation (1) is modified during propagation due to Compton scattering (see Section 2).

for Thomson scattering of $\tau_T \simeq 530$). Using this radius, Equation (1), and Monte Carlo method in Ramaty & Meszaros (1981), the photon spectrum can be calculated analytically (see gray dotted line in Figure 1).

The time dependence of the integral range is ignored, and we assume that photons emitted from the spherical shell are observed simultaneously. This assumption is justified as follows. For the parameter regime considered in this study, the photospheric radius is approximately $r_{\text{ph}} \sim 10^7$ cm and the Lorentz factor of the photospheric radius is $\Gamma_{\text{ph}} \sim 10$. Photons emitted from this photospheric radius at a given time are observed over a timescale of $t \sim r_{\text{ph}}/(c\Gamma_{\text{ph}}^2) \sim 10^{-6}$ s, which would be smaller than the time resolution of detectors. As a result, photons emitted from r_{ph} at a given time will fall within the same time bin of a detector and will be observed simultaneously. Consequently, it is not necessary to account for the delayed arrival of high-latitude emission, which is significant in the case of GRBs (Granot et al. 1999).

The line-like photon distribution function produces a power-law observed spectrum with a photon index of -1 . To demonstrate this, we adopt, for simplicity, a Gaussian distribution with mean $\varepsilon'_{\text{line}}$ and standard deviation $\varepsilon'_{\text{line}}\sigma$, as the distribution function. For this photon distribution function, the resulting spectrum is (see Appendix A for details),

$$F_\varepsilon \propto \varepsilon^2 \int_{x_c}^{x_j} dx \left[1 - \frac{\varepsilon'_{\text{line}}}{\varepsilon\Gamma} (x+1) \right] \exp \left[\frac{-x^2}{2\sigma^2} \right], \quad (2)$$

where $x_c = \varepsilon\Gamma(1-\beta)/\varepsilon'_{\text{line}} - 1$ and $x_j = \varepsilon\Gamma(1-\beta\mu_j)/\varepsilon'_{\text{line}} - 1$. Because of the Gaussian dependence on x in Equation (2), the dominant contribution to the integral arises at $x \sim 0$. In this regime, the multiplicative factor preceding the exponential function in the integrand of Equation (2) becomes $1 - \varepsilon'_{\text{line}}/(\varepsilon\Gamma) \sim 1 + \mathcal{O}(\Gamma^{-1})$ for $\varepsilon \gtrsim \varepsilon'_{\text{line}}$. Therefore, the integral becomes nearly independent of ε for $\varepsilon \gtrsim \varepsilon'_{\text{line}}$, provided that $x = 0$ lies within the integration domain. In this parameter regime, F_ε scales as ε^2 , resulting in a power-law spectrum with an index of 2, which corresponds to the photon index of -1 .¹ For ε satisfying $x_c > 0$, the flux suddenly decreases since the $x \sim 0$ lies outside the integral range. This condition gives an upper cut-off energy of $\varepsilon = 2\Gamma\varepsilon'_{\text{line}}$. Therefore, the power-law and cut-off spectrum is formed solely by the geometrical considerations, although it can be modified by further scatterings.

The spectrum of the line emission, which is originally characterized by $F_\varepsilon \propto \varepsilon^2$, can be modified during propagation through the surrounding plasma due to Compton scattering. Assuming a cold electron population, the optical depth for Compton scattering is given by (Abramowicz et al. 1991),

$$\tau_C = \int_r^{D_1} \frac{dr}{\mu} \Gamma(1-\beta\mu) \sigma_{e\gamma} n_\pm(r), \quad (3)$$

where $\sigma_{e\gamma}$ is scattering cross section for Compton scattering, and $n_\pm(r)$ is the electron-positron number density in the plasma comoving frame. For $\Theta = \cos^{-1}\mu \ll 1$ and $\Gamma \gg 1$, the factor $\Gamma(1-\beta\mu)$ in Equation (3) can be expressed as $\Gamma^{-1} (1 + (\Gamma\Theta)^2)/2$. In the regime $\Theta < \Gamma^{-1}$, this reduces to $\sim \Gamma^{-1}$, substantially suppressing the scattering. In contrast, for $\Theta \geq \Gamma^{-1}$, the factor becomes $\sim \Gamma\Theta^2$ increasing with the angle Θ . As a result, photons originating from high latitudes are more frequently scattered by the plasma, resulting in the modification of the initial spectrum. This modification will be numerically confirmed in Section 3.

3. NUMERICAL CALCULATION

In this section, we present detailed radiative transfer simulations of line emission from fireballs associated with MGFs. Using a Monte Carlo method, we model the evolution of the photon field under electron-positron pair annihilation, Compton scattering, and pair production processes. The simulations reveal a characteristic spectrum near 10 MeV. We evaluate the detectability of this spectral feature with current and future gamma-ray observatories, demonstrating that instruments such

¹ The specific flux F_ε is proportional to $\varepsilon(dN/d\varepsilon) \propto \varepsilon^{1-\gamma}$.

as the *Fermi*/GBM, e-ASTROGAM, GRAMS (Gamma-Ray and AntiMatter Survey), and the All-sky Medium Energy Gamma-ray Observatory eXplorer (AMEGO-X) have sufficient sensitivity to observe the predicted MeV emission from Galactic MGFs.

The numerical calculations are performed as follows (see Appendix B for details). The plasma profile is based on analytic solutions for a baryon-loaded fireball. Given the isotropic luminosity L_{iso} , the initial fireball radius r_0 , its thickness Δr , and amount of baryons, the plasma evolution is uniquely determined. Electron-positron pair annihilation (photon injection) is implemented using the Monte-Carlo method described by Ramaty & Meszaros (1981). At each simulation timestep, the radial positions of photon injection are randomly sampled according to the pair annihilation rate within each cell. Once injected, photons propagate outward and either escape the computational domain or are annihilated via pair production. The optical depth and scattering processes are evaluated following the prescriptions in Abramowicz et al. (1991); Pozdnyakov et al. (1983). Electron-positron pair production is treated iteratively using the optical depth formula of Gould & Schréder (1967) (see also e.g., Iwamoto & Takahara 2004, for details of the iterative procedure). The resulting photon distribution function obtained from each simulation is used in the subsequent simulation to evaluate the probability of pair production. This procedure is repeated iteratively until the photon spectrum in 2–20 MeV is converged (see Appendix B for details). To minimize uncertainties associated with the location of the inner boundary, we progressively shifted the boundary inward until the spectral results converged. The fluence of the line emission is hard to evaluate analytically since it depends on the anisotropic photon field created by pair annihilation and elementary processes in the anisotropic photon field. We calculate this fluence numerically using the iterative procedure for both the photon field and the inner boundary.

The adopted parameters are an isotropic-equivalent luminosity of $L_{\text{iso}} = 10^{47} \text{ erg s}^{-1}$, corresponding to the brightest MGF observed to date, an initial size of the fireball of $r_0 = 10^6 \text{ cm}$, and an observed burst duration of $\Delta t = 0.1 \text{ s}$. The shell width Δr is adjusted to reproduce the observed burst duration. For these parameters, the initial temperature of the fireball is 190 keV. The luminosity distance to the magnetar is assumed to be $D_l = 10 \text{ kpc}$. The dimensionless enthalpy η , which is the radiation energy density divided by the baryon rest-mass energy density, is set to be $10^2, 10^4, 10^8$. For $\eta = 10^8$, the baryonic component is negligible in terms of mass and number density, and thus the same as the purely pair fireball. The case with $\eta = 10^2$ is just between the

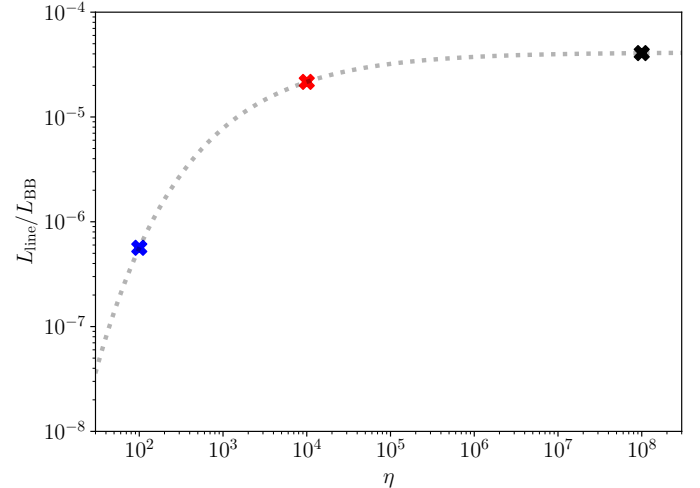


Figure 2. η -dependence of the line luminosity L_{line} normalized by the blackbody luminosity L_{BB} . The color scheme follows that of Figure 1 for ease of comparison.

radiation-dominated fireball and baryon-dominated fireball at the photospheric radius. The timescale of pair annihilation for electrons is smaller than the dynamical timescale in $r < r_{\text{an}} = 8.2r_0$, and this value is almost independent of η (see Appendix B for details). The photospheric radii defined by the Thomson cross section are at $r_{\text{ph}}/r_0 = 8.8, 19, 86$ for the cases of $\eta = 10^8, 10^4, 10^2$, respectively. At each of these radii, the bulk Lorentz factors are 11, 23, and 105.

In Figure 1, the black, red, and blue solid line shows the observed gamma-ray fluence for the cases of $\eta = 10^8, 10^4, 10^2$, respectively. The black dashed line indicates the primary blackbody component emitted from the fireball. The gray dotted line shows the result of the analytic model with $r_{\text{em}}/r_0 = 7.5$ (Equation 1). For the cases of $\eta = 10^8, 10^4$, owing to the relativistic Doppler shift, the peak of the line emission appears at $\sim 2\Gamma_{\text{em}}m_ec^2 \sim 10 \text{ MeV}$. The power-law spectrum is further modified below $\sim 5 \text{ MeV}$ due to Compton scattering, as described below Equation (3). This down-scattering softens the spectrum relative to the prediction of Equation (2), although emission in this energy range is dominated by the primary blackbody component and cannot be observable. In MGFs, the emission arising from electron-positron pair annihilation appears around 10 MeV as an additional component characterized by a power-law shape with an exponential cutoff, rather than a pure line feature.

The fewer baryons are present, the brighter the MeV photons become. The reason is as follows. If baryons exist, the associated electrons make the fireball optically thick far beyond r_{an} . In this region, the high-energy

Table 1. Expected photon counts in each energy band of e-ASTROGAM.

Energy Band	Effective Area	Photon Counts	
(MeV)	(cm ²)	$\eta = 10^8$	$\eta = 10^4$
5.0–15	50	120	58
7.5–15	215	160	71
15–40	846	0.1	0.07

NOTE—The photons in the first row is detected via Compton scattering, and those in the last two rows via pair production. Effective areas are taken from [de Angelis et al. \(2018\)](#).

photons are cooled through Compton scatterings with non-relativistic electrons.² Since the production rate of high-energy photons does not depend on the specific enthalpy η (see Appendix A for details), no additional high-energy photons are generated outside r_{an} in each model. Consequently, the presence of baryons only leads to the cooling of photon energies. Moreover, the isotropized high-energy photons can be absorbed more efficiently via pair production due to the larger angle between wave vectors. Figure 2 shows the luminosity ratios of the line component, defined as the component brighter than the blackbody above 1 MeV, to the blackbody component. The dashed line shows a numerical fitting by

$$\frac{L_{\text{line}}}{L_{\text{BB}}} = \mathcal{R} \exp \left[- \left(\frac{\eta_c}{\eta} \right)^s \right], \quad (4)$$

where $\mathcal{R} = 4.1 \times 10^{-5}$, $\eta_c = 3.5 \times 10^3$, and $s = 0.41$ are adopted.

This line component associated with an initial spike of an MGF could be observable with current and future gamma-ray telescopes, although the detectability depends on the amount of baryons. The GBM on board the *Fermi* satellite is a potential instrument for detecting this line emission ([Meegan et al. 2009](#)). The fluence of the line component shown in Figure 1 is comparable to the Ravasio line reported in GRB 221009A ([Ravasio et al. 2024; Zhang et al. 2024a; Burns et al. 2024](#)). Thus, assuming that the observational instrument is not significantly affected by the primary blackbody component, this line component should be detectable with this existing facility. More promising instruments are e-

² For photons with an energy of $m_e c^2$ in the comoving frame, the optical depth calculated using the Klein-Nishina cross section at radius r_{an} is 0.5, 8.8, and 880 for the cases of $\eta = 10^8$, 10^4 , and 10^2 , respectively.

ASTROGAM ([De Angelis et al. 2017; de Angelis et al. 2018](#)), GRAMS ([Aramaki et al. 2020](#)), and AMEGO-X ([Caputo et al. 2022](#)), planned space missions dedicated to MeV-GeV gamma-ray astrophysics. Table 1 shows the expected photon counts in each energy band based on the effective area of e-ASTROGAM (Tables 1.3.1 and 1.3.2 in [de Angelis et al. 2018](#)). The 1σ energy resolution of e-ASTROGAM at 10 MeV is expected to be less than 0.1 MeV, which will enable the detection of the power-law spectral shape predicted in this study. At 10 MeV, the effective areas of AMEGO-X and GRAMS range from 20 cm² to 200 cm² (see Figure 4 of [Aramaki et al. 2020](#) and Figure 12 of [Caputo et al. 2022](#)). Thus, both detectors are also capable of detecting $\mathcal{O}(100)$ photons from MGFs. Accordingly, the detection of an additional component in the MeV range, originating from the initial spike of a Galactic MGF and characterized by a power law plus an exponential cutoff, is expected to yield approximately $\mathcal{O}(100)$ photons collected within a 0.1 s interval.

4. SUMMARY AND DISCUSSION

In this paper, we have studied the photon spectrum of electron-positron pair annihilation line emission in MGFs. In section 2, we calculate the observed spectral shape under the assumptions that photons are emitted from a single shell moving at a relativistic velocity and that all photons are observed simultaneously. Through analytic calculations, we have shown that the spectrum becomes a power-law distribution with the peak energy at $2\Gamma\varepsilon'_{\text{line}}$. In section 3, we investigated the spectral properties using Monte Carlo radiative transfer simulations. The calculations included electron-positron annihilation, Compton scattering, and pair production. Iteratively evolving the photon field until convergence enable us to calculate the exact fluence for this line component. The obtained spectrum is in agreement with the analytic model, with small modification due to the Compton scattering.

This line emission component from MGFs is potentially detectable with current instruments such as the *Fermi*/GBM, although the detectability depends on the specific enthalpy of the fireball. The proposed MeV gamma-ray satellites, such as e-ASTROGAM, GRAMS, and AMEGO-X with high energy resolution and sensitivity in the MeV range, is expected to detect $\mathcal{O}(100)$ photons from such events, enabling identification of the predicted power-law spectrum with an exponential cutoff.

This MeV component has not been reported so far. There are several possible reasons for this. First, the most recent Galactic MGF from SGR 1806-20, which

occurred in late 2004, took place before the launch of the *Fermi* satellite in 2008. Second, the previous MGF likely involved a large baryon loading, resulting in weak emission in the MeV range. Given the limited number of observed MGFs, the possibility of future MGFs with small specific enthalpy cannot be excluded. On the contrary, MeV observation will independently provide valuable constraints on the baryon loading of MGFs, complementing the X-ray polarization approach for MSBs (Wada 2025). Third, no previous research has focused on the MeV emission of the initial spike of MGFs. Gamma-ray emission from the MGFs in the 0.1–10 MeV range is reported in Mereghetti et al. (2005); Frederiks et al. (2007); Boggs et al. (2007). However, their analyses targeted the pulsating tail and later phases, rather than the initial spike. In these phases, MeV photons may result from low-energy photons from a trapped fireball being up-scattered (e.g., Yamasaki et al. 2020), or may originate from the decay of r-process elements (Patel et al. 2025). Our study underscores the importance of MeV gamma-ray observation of the initial spike of MGFs.

The observed spectrum may exhibit variations due to unconsidered parameters in this study. Radio afterglow observations of an MGF from SGR 1806-20 (Gaensler et al. 2005; Cameron et al. 2005) suggest that relativistic outflows associated with MGFs can contain a baryonic component (Nakar et al. 2005). The presence of this baryonic component can modify the line spectrum, as MeV photons undergo scattering by the electrons associated with the baryonic component (Shemi & Piran 1990; Meszaros et al. 1993; Mészáros & Rees 2000). This scattering process could lead to a softening of the spectrum, particularly at lower energies. Fur-

thermore, the isotropic-equivalent luminosity can vary considerably. Our current analysis focuses on most optimistic case observed to date. These parameters will be studied in our future studies.

Reproducing the Ravasio line within a simple fireball scenario is unlikely. To produce a ~ 10 MeV line at the maximal isotropic luminosity of $L_{\text{iso}} = 10^{54} \text{ erg s}^{-1}$, the initial radius must be $r_0 \simeq 10^9 \text{ cm}$, otherwise the value of Lorentz factor at the emission region would be far from the suitable value of $\Gamma_{\text{em}} \sim 20$. Numerical calculations with this setup yield a line flux of $L_{\text{iso}} \simeq 10^{48} \text{ erg s}^{-1}$, or $\sim 10^{-6}$ times the primary blackbody component. In contrast, the observed Ravasio line reaches $\sim 10^{-2}$ times the primary component, ruling out a pure fireball origin.

We thank K. Asano, K. Ioka, W. Ishizaki, R. Kuze, R. Matsui, K. Murase, and K. Toma for fruitful discussions, comments. We also thank the anonymous referee for many valuable comments that helped improve the manuscript. This work is supported by Grants-in-Aid for Scientific Research, Nos. 22K20366, 23H04899, 25KJ0024, 25K17378 (T.W.), 22K14028, 21H04487, 23H04899 (S.S.K.) from the Ministry of Education, Culture, Sports, Science and Technology (MEXT) of Japan. S.S.K. acknowledges the support by the Tohoku Initiative for Fostering Global Researchers for Interdisciplinary Sciences (TI-FRIS) of MEXT’s Strategic Professional Development Program for Young Researchers. Discussions during the YITP workshop YITP-W-24-22 on “Exploring Extreme Transients” at the Yukawa Institute for Theoretical Physics in Kyoto University (YITP) were useful in completing this work. The numerical calculations were carried out on Yukawa-21 at YITP and Cray XD2000 at the Center for Computational Astrophysics, National Astronomical Observatory of Japan.

APPENDIX

A. DERIVATION OF OBSERVED SPECTRUM

In this section, we derive the relation between the photon distribution function and the observed spectrum given in Equation (1). Following the approach in Section 2, we assume that photons are emitted from a spherically expanding, relativistic single shell at r_{em} , with Lorentz factor Γ_{em} .

For a spherically symmetric system in real space, a photon distribution function can be expressed as $f(\varepsilon, \mu; r)$, where ε is the photon energy, μ is the cosine of the angle between the radial direction and the photon momentum, and r is the radial coordinate (see Figure 3). This distribution function is Lorentz invariant and is re-

lated to the specific intensity I_ε , by $I_\varepsilon = \varepsilon^3 f/c^2$ (e.g., Rybicki & Lightman 1979). The observer is located at $r = D_1$. According to Liouville’s theorem, the distribution function is conserved along photon trajectories, yielding (Li & Sari 2008)

$$f(\varepsilon', \mu'; r_{\text{em}}) = f(\varepsilon, \mu; r_{\text{em}}) = f(\varepsilon_o, \mu_o; D_1), \quad (\text{A1})$$

where primed quantities refer to values in the comoving frame of the shell, and the subscript ‘o’ refers to values in the laboratory frame at the observer position (see Figure 3). The first equality in Equation (A1) arises from the Lorentz invariance of the distribution function, and the second one from Liouville’s theorem. Note that

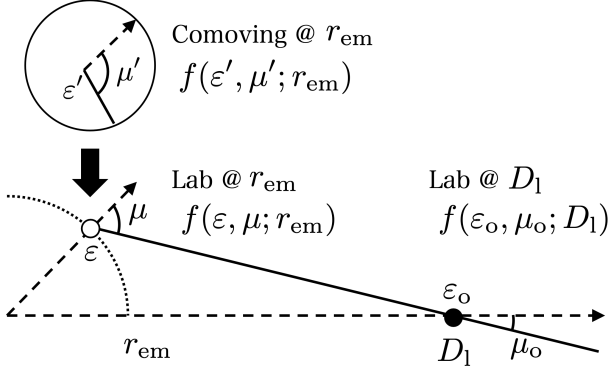


Figure 3. Schematic diagram of the variables in Equation (A1). A photon is emitted at r_{em} isotropically in the plasma comoving frame and is observed at D_1 .

the argument in $f(\varepsilon', \mu'; r_{\text{em}})$ includes variables in both the plasma comoving frame (ε', μ') and the laboratory frame r_{em} , as is often adopted (e.g., Li & Sari 2008; Beloborodov 2011).

The observed spectrum is a superposition of photons, with varying beaming factors, over the entire shell. Using the distribution function, we can calculate the observed specific flux as follows. The observed specific flux is

$$F_{\varepsilon_o} = c^{-2} \int d\Omega_o \varepsilon_o^3 f(\varepsilon_o, \mu_o; D_1) \mu_o \\ = \frac{2\pi}{c^2} \left(\frac{r_{\text{em}}}{D_1} \right)^2 \int_{\mu_j}^1 d\mu \mu \varepsilon_o^3 f(\varepsilon_o, \mu; r_{\text{em}}) \quad (\text{A2})$$

where we have used Equation (A1), $\mu_o^2 = 1 - (r_{\text{em}}/D_1)^2(1 - \mu^2)$ (e.g. Rybicki & Lightman 1979), and $\varepsilon_o = \varepsilon$. The integral range of μ is determined by the geometry of the emitting shell. Thus, Equation (1) is derived.

Let us assume that the distribution function in the comoving frame is isotropic and Gaussian, and derive a power-law distribution of observed spectrum (see Figures 2 and 3 in Ramaty & Meszaros 1981 for the spectral line profile adopted in our simulation). The mean and standard deviation of the distribution function are set to be $\varepsilon'_{\text{line}}$ and $\varepsilon'_{\text{line}}\sigma$. The distribution function is expressed as

$$f_G(\varepsilon') = \frac{\mathcal{F}_0}{\sqrt{2\pi\sigma^2}} \exp \left[-\frac{(\varepsilon'/\varepsilon'_{\text{line}} - 1)^2}{2\sigma^2} \right], \quad (\text{A3})$$

where \mathcal{F}_0 is a constant representing the photon number density. For $\sigma \ll 1$, the photon number density in real space is given by $4\pi c^{-3} \varepsilon'_{\text{line}}^3 \mathcal{F}_0$. For an isotropic distribution in the comoving frame, $f(\varepsilon', \mu'; r_{\text{em}})$ is independent of μ' and can be expressed as $f_G(\varepsilon')$ at

$r = r_{\text{em}}$. Using Equation (A1) together with the relation $\varepsilon' = \varepsilon_o \Gamma(1 - \beta\mu)$, Equation (A2) can be rewritten as

$$F_{\varepsilon_o} = \frac{2\pi}{c^2} \left(\frac{r_{\text{em}}}{D_1} \right)^2 \int_{\mu_j}^1 d\mu \mu \varepsilon_o^3 f_G(\varepsilon_o \Gamma(1 - \beta\mu)). \quad (\text{A4})$$

Substituting a gaussian distribution (see Equation A3) into this expression, we obtain the observed spectrum as follows,

$$F_{\varepsilon_o} = \frac{2\pi}{c^2} \left(\frac{r_{\text{em}}}{D_1} \right)^2 \int_{\mu_j}^1 d\mu \mu \varepsilon_o^3 \frac{\mathcal{F}_0}{\sqrt{2\pi\sigma^2}} \\ \times \exp \left[-\frac{(\varepsilon_o \Gamma(1 - \beta\mu)/\varepsilon'_{\text{line}} - 1)^2}{2\sigma^2} \right] \\ = \frac{\sqrt{2\pi}}{c^2 \sigma} \left(\frac{r_{\text{em}}}{D_1} \right)^2 \frac{\varepsilon'_{\text{line}}}{\Gamma \beta^2} \varepsilon_o^2 \mathcal{F}_0 \\ \times \int_{x_c}^{x_j} dx \left[1 - \frac{\varepsilon'_{\text{line}}}{\varepsilon_o \Gamma} (x + 1) \right] \exp \left[\frac{-x^2}{2\sigma^2} \right], \quad (\text{A5})$$

where the integral variable μ is transformed to x using the relation $x = \varepsilon_o \Gamma(1 - \beta\mu)/\varepsilon'_{\text{line}} - 1$. The integral range for x is from $x_c = \varepsilon_o \Gamma(1 - \beta)/\varepsilon'_{\text{line}} - 1$ to $x_j = \varepsilon_o \Gamma(1 - \beta\mu_j)/\varepsilon'_{\text{line}} - 1$. Rewriting ε_o as ε and substituting $\beta = 1$, we obtain Equation (2).

The spectral shape is determined by the order of magnitude of x_c , 0, and x_j . The integral domain is

$$\frac{\varepsilon \Gamma(1 - \beta)}{\varepsilon'_{\text{line}}} - 1 \leq x \leq \frac{\varepsilon \Gamma(1 - \beta\mu_j)}{\varepsilon'_{\text{line}}} - 1, \quad (\text{A6})$$

which is determined by the angular size of the shell $1 \geq \mu \geq \mu_j$. The dominant contribution to the integral arises around $x \sim 0$. As mentioned in Section 2, if $x_c \lesssim 0 \lesssim x_j$ is satisfied, the integral becomes nearly independent of ε resulting in $F_\varepsilon \propto \varepsilon^2$. At lower energies, the spectrum begins to slightly deviate from this power-law around $\varepsilon \sim \varepsilon'_{\text{line}}$, and exhibits a sudden decline at the energy where $0 > x_j$ is satisfied. The upper cutoff energy appears at the energy where $0 < x_c$ is satisfied. Therefore, cutoff occurs outside the following energy range:

$$\frac{\varepsilon'_{\text{line}}}{\Gamma(1 - \beta\mu_j)} \leq \varepsilon \lesssim 2\Gamma\varepsilon'_{\text{line}}, \quad (\text{A7})$$

the spectrum where we have used $(1 - \beta)^{-1} \simeq 2\Gamma^2$ for $\Gamma \gg 1$. Within this energy range, the power-law spectrum is formed. For $\varepsilon'_{\text{line}} = 511 \text{ keV}$, $\Gamma = 10$, and $\mu_j = 0$, the upper cutoff is approximately 10 MeV, and the lower cutoff is about 50 keV.

B. DETAILS OF NUMERICAL CALCULATION

We solve the radiative transfer using a Monte-Carlo scheme applied to the plasma flow described by the analytic solution of relativistic fireballs. In this section, we describe the analytic solution for a baryon-loaded fireball, which is adopted in this study, and describes the details of the numerical method. In this paper, we focus on the parameter regime where the radiation energy density at the photospheric radius exceeds the baryon rest-mass energy density, as this condition is required to produce the blackbody radiation observed in MGPs.

The analytic solution for a baryon-loaded fireball is summarized below (see Paczynski 1986; Shemi & Piran 1990; Meszaros et al. 1993; Mészáros & Rees 2000; see e.g., Piran 1999; Zhang 2018 for reviews). The fireball dynamics are determined by the isotropic luminosity, L_{iso} , the initial radius, r_0 , initial baryon-mass density, ρ_0 , and the width of a shell, Δr . To describe the dynamics and thermodynamics of an optically thick fireball, we adopt a one-component fluid approximation under the assumption that the plasma and radiation are in thermal equilibrium initially. For a given isotropic-equivalent luminosity L_{iso} , initial radius r_0 , and initial Lorentz factor Γ_0 , the initial temperature of the fireball is determined as

$$T_0 = \left(\frac{L_{\text{iso}}}{4\pi r_0^2 c a_{\text{rad}} \Gamma_0^2} \right)^{1/4} \sim 190 \text{ keV } L_{\text{iso},47}^{1/4}, \quad (\text{B8})$$

where a_{rad} is the radiation constant, and T_0 has the dimension of energy. Assuming that the transonic point lies sufficiently deep inside, the velocity at r_0 is taken to be the sound speed of a radiation-dominated gas, $c/\sqrt{3}$, resulting in $\Gamma_0 = \sqrt{3}/2$. The dimensionless enthalpy η is defined as

$$\eta = \frac{a_{\text{rad}} T_0^4}{\rho_0 c^2}. \quad (\text{B9})$$

In the ultrarelativistic limit during the acceleration phase (see e.g., Piran 1999; Zhang 2018 for the coasting phase), the fireball's bulk Lorentz factor Γ , comoving temperature T , baryon-mass density ρ , and positron number density n_+ evolve as (e.g., Paczynski 1986; Piran 1999; Zhang 2018, see also Section 105 of Landau & Lifshitz 1980 for Equation B13)

$$\Gamma = \Gamma_0 \bar{r}, \quad (\text{B10})$$

$$T = T_0 \bar{r}^{-1}, \quad (\text{B11})$$

$$\rho = \rho_0 \bar{r}^{-3}, \quad (\text{B12})$$

$$n_+ = -\frac{\rho}{2m_p} + \left[\frac{\rho^2}{4m_p^2} + 4 \left(\frac{m_e T}{2\pi\hbar^2} \right)^3 e^{-2m_e c^2/T} \right]^{1/2}, \quad (\text{B13})$$

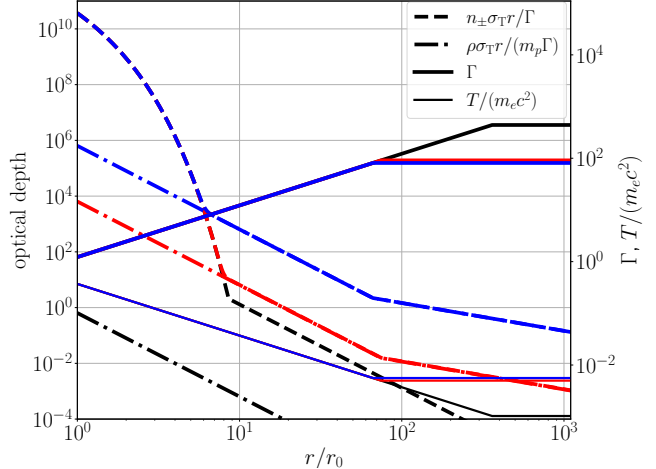


Figure 4. Radial dependences of optical depth for Thomson scattering (dashed lines for the total electron-positron population and dash-dotted lines for electrons associated with the baryonic component), Lorentz factor (thick solid lines), and comoving temperature (thin solid lines). The color scheme follows that of Figure 1, i.e., black, red, and blue lines correspond to the cases with $\eta = 10^8$, 10^4 , and 10^2 , respectively.

where \hbar is the reduced Planck constant and $\bar{r} = r/r_0$. From charge neutrality, the electron number density n_- is given by $n_- = n_+ + \rho/m_p$. The radial dependences of these values are shown in Figure 4. As indicated by Equation (B13), the positron number density exhibits a complex dependence on \bar{r} . However, in the limit where the baryon number density is negligible compared to that of the positrons, the relation simplifies to $n_+ \propto \bar{r}^{-3/2} \exp(-m_e c^2 T_0^{-1} \bar{r})$, depending on the radius exponentially. We note that the product $n_+ n_-$, which determines the pair-annihilation rate, does not depend on the baryon number density ρ/m_p . This is because the electron and positron chemical potentials μ_- , μ_+ satisfy $\mu_+ + \mu_- = 0$, and the factor involving the chemical potentials in the number densities, $n_+ n_- \propto \exp[(\mu_+ + \mu_-)/T]$, cancel out.

The photons escape from the radius where the optical depth for Thomson scattering is approximately unity. For electrons associated with the baryonic component, the photospheric radius is defined by the condition $\sigma_T(\rho/m_p)r/\Gamma = 1$, which yields a photospheric radius for baryonic component,

$$\bar{r}_{\text{ph,baryon}} = \left(\frac{\sigma_T L_{\text{iso}}}{4\pi m_p r_0 c^3 \Gamma_0^3 \eta} \right)^{1/3} \sim 86 L_{\text{iso},47}^{1/3} \eta_{,2}^{-1/3}. \quad (\text{B14})$$

Similarly, for the pair component, the photospheric radius is defined by $\sigma_T 2n_+ r/\Gamma = 1$. In the regime where the baryon number density is negligible compared to

the pair number density, n_+ is dominated by an exponential dependence on T (see Equation B13); consequently the temperature at the photospheric radius depends weakly on other parameters. Defining the temperature at this radius as $T_{\text{ph,pair}}$ and neglecting the logarithmic parameter dependence in the pair number density (see Equation B13), the photospheric radius for pair component is given by

$$\bar{r}_{\text{ph,pair}} \simeq \frac{T_0}{T_{\text{ph,pair}}} \sim 8.8 L_{\text{iso},47}^{1/4}, \quad (\text{B15})$$

where we adopt a fiducial value of $T_{\text{ph,pair}} = 22 \text{ keV}$, which has a weak logarithmic dependence on L_{iso} , r_0 , and η .

Beyond the annihilation radius r_{an} , where the timescale of pair annihilation for positrons becomes comparable to the dynamical timescale, the positron number density freezes out, and the single-component approximation breaks down. This radius is determined by the condition $(\sigma_{+-} c \beta_e n_-)^{-1} \simeq r/(c\Gamma)$, where β_e is the thermal velocity of the pairs normalized by the speed of light. In the non-relativistic limit ($\beta_e \ll 1$), the pair-annihilation cross section is approximated by $\sigma_{+-} \simeq 3\sigma_T/(8\beta_e)$. Assuming that the baryon number density is negligible compared to the pair number density, same as in Equation (B15), this radius is mainly determined by the temperature of the plasma, and the annihilation radius is given by

$$r_{\text{an}} \simeq \frac{T_0}{T_{\text{an,pair}}} \sim 8.2 L_{\text{iso},47}^{1/4}, \quad (\text{B16})$$

where $T_{\text{an,pair}} = 23 \text{ keV}$, which also has a weak logarithmic dependence on parameters, is adopted. In this parameter regime, Equation (B13) is no longer valid. Beyond this radius, the positron number density is determined by the conservation of number flux:

$$n_+ = n_{+,\text{an}} \frac{\Gamma_{\text{an}} r_{\text{an}}^2}{\Gamma r^2}, \quad (\text{B17})$$

where subscript ‘an’ denotes the value at r_{an} .

Above the photospheric radius, the plasma continues to be accelerated by scattering of the escaping photons. Photons decouple from the fireball at the photospheric radius r_{ph} , which is defined using the total electron-positron number density $n_{\pm} = n_- + n_+$ and well approximated by $r_{\text{ph}} \simeq \max(r_{\text{ph,pair}}, r_{\text{ph,baryon}})$, but the scaling relations in Equations (B10) still hold. The acceleration above r_{ph} occurs because the pair plasma is accelerated via scattering by the escaping photons, which dominate the energy density, as long as the photospheric luminosity exceeds the kinetic luminosity of the plasma (Grimsrud & Wasserman 1998; Li & Sari 2008; Chhotray &

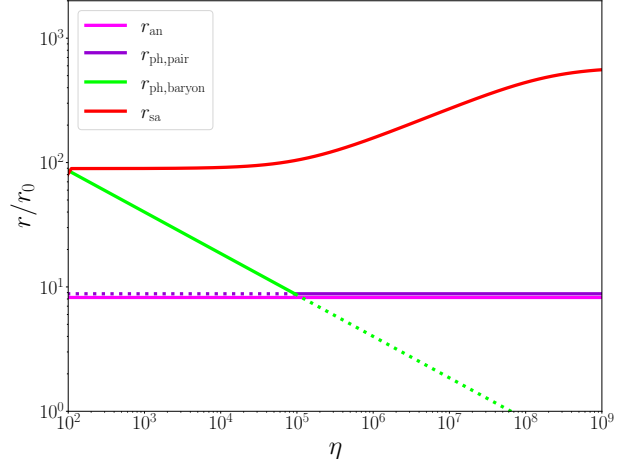


Figure 5. η -dependence of each radius. $r_{\text{ph,pair}}$ and $r_{\text{ph,baryon}}$ are photospheric radii for pair-plasma and baryonic component, respectively. The physically relevant photospheric radius $r_{\text{ph}} \simeq \max(r_{\text{ph,pair}}, r_{\text{ph,baryon}})$, is shown with solid green and purple lines; dotted lines show analytic expressions in regimes where the corresponding radii are not physically relevant.

Lazzati 2018). Above r_{ph} , the electron velocity distribution follow the Maxwell-Boltzmann distribution, normalized by the number density of Equation (B17). The acceleration by the radiation ceases at the saturation radius, where the work done by the radiation during the dynamical time in the comoving frame is equal to the rest mass energy of a particle (Meszaros et al. 1993; Grimsrud & Wasserman 1998; Nakar et al. 2005),

$$\bar{r}_{\text{sa}} = \left(\frac{L_{\text{iso}} \sigma_T}{4\pi \bar{m} c^3 r_0 \Gamma_0^3} \right)^{1/4} \sim 90 L_{\text{iso},47}^{1/4} \left(\frac{m_p}{\bar{m}} \right)^{1/4}, \quad (\text{B18})$$

where $\bar{m} = (\rho + m_e n_- + m_e n_+)/(\rho/m_p + n_- + n_+)$ is the average particle mass. Shell spreading begins at $r \sim \bar{r}_{\text{sa}}^2 \Delta r$, but this radius lies far beyond the region of interest in this study. η -dependence of these radii are summarized in Figure 5.

On this analytic plasma profile, we solved the photon propagation numerically. In our Monte-Carlo scheme, the radiation field is represented by a collection of photon packets, each carrying information on position, momentum, and number of photons in the packet (see e.g., Dolence et al. 2009; Lazzati 2016; Kawaguchi et al. 2023). The radial direction is discretized into $N_r = 4000$ spatial cells on a logarithmic scale. Within each cell, the analytic solutions for T , n_{\pm} , ρ , and Γ , along with the local mean free path for photon pair production are provided. The optical depth for photon-photon annihilation depends on both the photon frequency and its propagation direction. The frequency is discretized log-

arithmically over the range $10^{-3}m_ec^2$ to $10^3m_ec^2$ with 10000 bins, while the propagation direction is discretized uniformly in cosine, also with 10000 bins. For the optical depth calculation of pair production, both dimensions are coarsened into 100 cells each, and the values at midpoints are obtained via interpolation. Using the values, the optical depths for the scattering and pair production are evaluated at each time step.

We incorporate both the time dependence and photon annihilation via electron-positron pair production into the numerical simulation code developed in [Wada & Asano \(2025\)](#). The code has been validated against several benchmark problems: it reproduces the inverse-Comptonized spectrum in a static plasma as presented in [Pozdnyakov et al. \(1983\)](#); the relativistic beaming factor in an outflow as shown in [Beloborodov \(2011\)](#); the analytic solution for the radiation energy-momentum tensor in a relativistic outflow; and the analytic optical depth for pair production for the static, power-law photon distribution. The details of the scattering process are described in [Wada & Asano \(2025\)](#). The stochastic treatment of pair production and Compton scattering follows the prescription of [Iwamoto & Takahara \(2004\)](#), and the pair annihilation is incorporated via iterative procedures similar to those described therein. The location of the inner boundary is progressively shifted inward, starting from a radius corresponding to an optical depth for Thomson scattering of $\tau_T = 15$ until the spectral results converged around $\tau_T \simeq 4000$. We confirm that the numerical results converged within 10% accuracy in the energy range of 2–20 MeV.

The solid lines in Figure 6 show the pair-annihilation optical depth for photons emitted at radius r , as evaluated from the simulation results. Photons with $\varepsilon \geq m_ec^2$ are taken into account here. The energy of photons emitted at radius r is attenuated by a factor of $\exp(-\tau_{\gamma\gamma})$ at the outer edge of the simulation domain due to the pair annihilation. Pair-annihilation effects are more pronounced in baryon-rich fireballs. The optical depth

shown by the solid curve in Figure 6 is computed by dividing the radius into bins. For each bin, we define $E_{\text{inj}}(r)$ as the total energy of photons injected in the bin that would be observed with energies above m_ec^2 if they escaped freely, and $E_{\text{out}}(r)$ as the total energy of photons from the same region that are actually observed above m_ec^2 . The optical depth for pair-annihilation is then evaluated by $\tau_{\gamma\gamma}(r) = -\ln [E_{\text{out}}(r)/E_{\text{inj}}(r)]$. The dotted lines in Figure 6 show the radial dependence of the enclosed luminosity fraction, defined as the cumulative fraction of total radiated energy originating from within radius r . This quantity indicates the contribution of emission generated inside the radius r , $E_{r<}$, to the final energy output E_{tot} . For the $\eta = 10^2$ case (blue lines), although $\tau_{\gamma\gamma}$ is of order unity at $r \sim 20$ (blue solid line), the energy fraction originating from this radius is negligible (blue dotted line) and does not affect the observed spectrum.

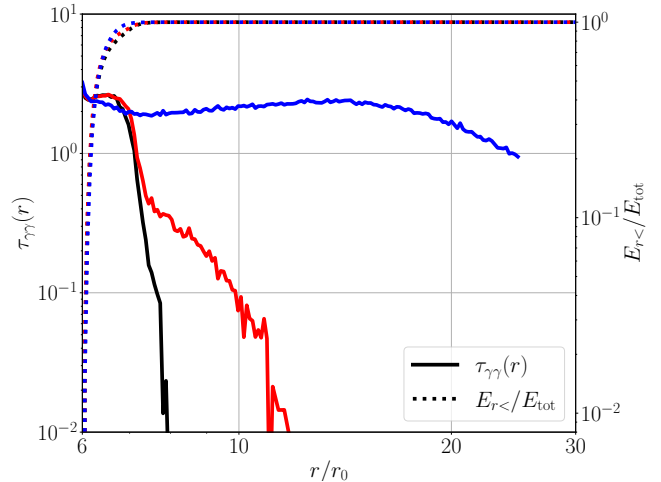


Figure 6. Radial dependence of pair-annihilation optical depth for photons emitted at the radius r (solid lines), and radial dependence of enclosed energy fraction (dotted lines). The color scheme follows those of Figures 1 and 4.

REFERENCES

- Abbasi, R., Ackermann, M., Adams, J., et al. 2023, ApJL, 946, L26, doi: [10.3847/2041-8213/acc077](https://doi.org/10.3847/2041-8213/acc077)
- Abramowicz, M. A., Novikov, I. D., & Paczynski, B. 1991, ApJ, 369, 175, doi: [10.1086/169748](https://doi.org/10.1086/169748)
- Ai, S., & Gao, H. 2023, ApJ, 944, 115, doi: [10.3847/1538-4357/acb3bf](https://doi.org/10.3847/1538-4357/acb3bf)
- An, Z.-H., Antier, S., Bi, X.-Z., et al. 2023, arXiv e-prints, arXiv:2303.01203, doi: [10.48550/arXiv.2303.01203](https://doi.org/10.48550/arXiv.2303.01203)
- Aramaki, T., Adrian, P. O. H., Karagiorgi, G., & Odaka, H. 2020, Astroparticle Physics, 114, 107, doi: [10.1016/j.astropartphys.2019.07.002](https://doi.org/10.1016/j.astropartphys.2019.07.002)
- Axelsson, M., Ajello, M., Arimoto, M., et al. 2024, arXiv e-prints, arXiv:2409.04580, doi: [10.48550/arXiv.2409.04580](https://doi.org/10.48550/arXiv.2409.04580)
- Beloborodov, A. M. 2011, ApJ, 737, 68, doi: [10.1088/0004-637X/737/2/68](https://doi.org/10.1088/0004-637X/737/2/68)
- Boggs, S. E., Zoglauer, A., Bellm, E., et al. 2007, ApJ, 661, 458, doi: [10.1086/516732](https://doi.org/10.1086/516732)

- Burns, E., Lesage, S., Goldstein, A., et al. 2024, arXiv e-prints, arXiv:2410.00286, doi: [10.48550/arXiv.2410.00286](https://doi.org/10.48550/arXiv.2410.00286)
- Cameron, P. B., Chandra, P., Ray, A., et al. 2005, *Nature*, 434, 1112, doi: [10.1038/nature03605](https://doi.org/10.1038/nature03605)
- Caputo, R., Ajello, M., Kierans, C. A., et al. 2022, *Journal of Astronomical Telescopes, Instruments, and Systems*, 8, 044003, doi: [10.1117/1.JATIS.8.4.044003](https://doi.org/10.1117/1.JATIS.8.4.044003)
- Chhotray, A., & Lazzati, D. 2018, *MNRAS*, 476, 2352, doi: [10.1093/mnras/sty286](https://doi.org/10.1093/mnras/sty286)
- Das, S., & Razzaque, S. 2023, *A&A*, 670, L12, doi: [10.1051/0004-6361/202245377](https://doi.org/10.1051/0004-6361/202245377)
- De Angelis, A., Tatischeff, V., Tavani, M., et al. 2017, *Experimental Astronomy*, 44, 25, doi: [10.1007/s10686-017-9533-6](https://doi.org/10.1007/s10686-017-9533-6)
- de Angelis, A., Tatischeff, V., Grenier, I. A., et al. 2018, *Journal of High Energy Astrophysics*, 19, 1, doi: [10.1016/j.jheap.2018.07.001](https://doi.org/10.1016/j.jheap.2018.07.001)
- Dolence, J. C., Gammie, C. F., Mościbrodzka, M., & Leung, P. K. 2009, *ApJS*, 184, 387, doi: [10.1088/0067-0049/184/2/387](https://doi.org/10.1088/0067-0049/184/2/387)
- Evans, W. D., Klebesadel, R. W., Laros, J. G., et al. 1980, *ApJL*, 237, L7, doi: [10.1086/183222](https://doi.org/10.1086/183222)
- Feroci, M., Frontera, F., Costa, E., et al. 1999, *ApJL*, 515, L9, doi: [10.1086/311964](https://doi.org/10.1086/311964)
- Frederiks, D., Svinkin, D., Lysenko, A. L., et al. 2023, *ApJL*, 949, L7, doi: [10.3847/2041-8213/acd1eb](https://doi.org/10.3847/2041-8213/acd1eb)
- Frederiks, D. D., Golenetskii, S. V., Palshin, V. D., et al. 2007, *Astronomy Letters*, 33, 1, doi: [10.1134/S106377370701001X](https://doi.org/10.1134/S106377370701001X)
- Gaensler, B. M., Kouveliotou, C., Gelfand, J. D., et al. 2005, *Nature*, 434, 1104, doi: [10.1038/nature03498](https://doi.org/10.1038/nature03498)
- Goodman, J. 1986, *ApJL*, 308, L47, doi: [10.1086/184741](https://doi.org/10.1086/184741)
- Gould, R. J., & Schréder, G. P. 1967, *Physical Review*, 155, 1404, doi: [10.1103/PhysRev.155.1404](https://doi.org/10.1103/PhysRev.155.1404)
- Granot, J., Piran, T., & Sari, R. 1999, *ApJ*, 513, 679, doi: [10.1086/306884](https://doi.org/10.1086/306884)
- Grimsrud, O. M., & Wasserman, I. 1998, *MNRAS*, 300, 1158, doi: [10.1046/j.1365-8711.1998.02004.x](https://doi.org/10.1046/j.1365-8711.1998.02004.x)
- Hurley, K., Cline, T., Mazets, E., et al. 1999, *Nature*, 397, 41, doi: [10.1038/16199](https://doi.org/10.1038/16199)
- Hurley, K., Boggs, S. E., Smith, D. M., et al. 2005, *Nature*, 434, 1098, doi: [10.1038/nature03519](https://doi.org/10.1038/nature03519)
- Ioka, K. 2020, *ApJL*, 904, L15, doi: [10.3847/2041-8213/abc6a3](https://doi.org/10.3847/2041-8213/abc6a3)
- Ioka, K., Murase, K., Toma, K., Nagataki, S., & Nakamura, T. 2007, *ApJL*, 670, L77, doi: [10.1086/524405](https://doi.org/10.1086/524405)
- Ito, H., Nagataki, S., Matsumoto, J., et al. 2014, *ApJ*, 789, 159, doi: [10.1088/0004-637X/789/2/159](https://doi.org/10.1088/0004-637X/789/2/159)
- Ito, H., Nagataki, S., Ono, M., et al. 2013, *ApJ*, 777, 62, doi: [10.1088/0004-637X/777/1/62](https://doi.org/10.1088/0004-637X/777/1/62)
- Iwamoto, S., & Takahara, F. 2004, *ApJ*, 601, 78, doi: [10.1086/380300](https://doi.org/10.1086/380300)
- Jiang, L.-Y., Wang, Y., Wei, Y.-J., et al. 2025, *Nature Communications*, 16, 2668, doi: [10.1038/s41467-025-57791-w](https://doi.org/10.1038/s41467-025-57791-w)
- Kann, D. A., Agayeva, S., Aivazyan, V., et al. 2023, *ApJL*, 948, L12, doi: [10.3847/2041-8213/acc8d0](https://doi.org/10.3847/2041-8213/acc8d0)
- Kaspi, V. M., & Beloborodov, A. M. 2017, *ARA&A*, 55, 261, doi: [10.1146/annurev-astro-081915-023329](https://doi.org/10.1146/annurev-astro-081915-023329)
- Kawaguchi, K., Fujibayashi, S., & Shibata, M. 2023, *PhRvD*, 107, 023026, doi: [10.1103/PhysRevD.107.023026](https://doi.org/10.1103/PhysRevD.107.023026)
- Kong, D.-F., Wang, X.-G., Zheng, W., et al. 2024, *ApJ*, 971, 56, doi: [10.3847/1538-4357/ad5ce1](https://doi.org/10.3847/1538-4357/ad5ce1)
- Kusafuka, Y., & Asano, K. 2025, *MNRAS*, 540, 2098, doi: [10.1093/mnras/staf879](https://doi.org/10.1093/mnras/staf879)
- Landau, L. D., & Lifshitz, E. M. 1980, *Statistical Physics* Part I, 3rd edn. (Amsterdam: Elsevier)
- Lazzati, D. 2016, *ApJ*, 829, 76, doi: [10.3847/0004-637X/829/2/76](https://doi.org/10.3847/0004-637X/829/2/76)
- Lesage, S., Veres, P., Briggs, M. S., et al. 2023, *ApJL*, 952, L42, doi: [10.3847/2041-8213/ace5b4](https://doi.org/10.3847/2041-8213/ace5b4)
- LHAASO Collaboration, Cao, Z., Aharonian, F., et al. 2023, *Science*, 380, 1390, doi: [10.1126/science.adg9328](https://doi.org/10.1126/science.adg9328)
- Li, C., & Sari, R. 2008, *ApJ*, 677, 425, doi: [10.1086/527551](https://doi.org/10.1086/527551)
- Liu, J., Mao, J., Xiong, S.-L., & Zhang, Y.-Q. 2025, arXiv e-prints, arXiv:2509.14715, doi: [10.48550/arXiv.2509.14715](https://doi.org/10.48550/arXiv.2509.14715)
- LST Collaboration, Abe, K., Abe, S., et al. 2025, arXiv e-prints, arXiv:2507.03077, <https://arxiv.org/abs/2507.03077>
- Malesani, D. B., Levan, A. J., Izzo, L., et al. 2023, arXiv e-prints, arXiv:2302.07891, doi: [10.48550/arXiv.2302.07891](https://doi.org/10.48550/arXiv.2302.07891)
- Meegan, C., Lichti, G., Bhat, P. N., et al. 2009, *ApJ*, 702, 791, doi: [10.1088/0004-637X/702/1/791](https://doi.org/10.1088/0004-637X/702/1/791)
- Mereghetti, S., Götz, D., von Kienlin, A., et al. 2005, *ApJL*, 624, L105, doi: [10.1086/430669](https://doi.org/10.1086/430669)
- Mereghetti, S., Rigoselli, M., Salvaterra, R., et al. 2024, *Nature*, 629, 58, doi: [10.1038/s41586-024-07285-4](https://doi.org/10.1038/s41586-024-07285-4)
- Meszaros, P., Laguna, P., & Rees, M. J. 1993, *ApJ*, 415, 181, doi: [10.1086/173154](https://doi.org/10.1086/173154)
- Mészáros, P., & Rees, M. J. 2000, *ApJ*, 530, 292, doi: [10.1086/308371](https://doi.org/10.1086/308371)
- Murase, K., & Ioka, K. 2008, *ApJ*, 676, 1123, doi: [10.1086/527667](https://doi.org/10.1086/527667)
- Murase, K., Mukhopadhyay, M., Kheirandish, A., Kimura, S. S., & Fang, K. 2022, *ApJL*, 941, L10, doi: [10.3847/2041-8213/aca3ae](https://doi.org/10.3847/2041-8213/aca3ae)

- Nakar, E., Piran, T., & Sari, R. 2005, *ApJ*, 635, 516, doi: [10.1086/497296](https://doi.org/10.1086/497296)
- Paczynski, B. 1986, *ApJL*, 308, L43, doi: [10.1086/184740](https://doi.org/10.1086/184740)
- Patel, A., Metzger, B. D., Cehula, J., et al. 2025, *ApJL*, 984, L29, doi: [10.3847/2041-8213/adc9b0](https://doi.org/10.3847/2041-8213/adc9b0)
- Pe'er, A., Mészáros, P., & Rees, M. J. 2006, *ApJ*, 642, 995, doi: [10.1086/501424](https://doi.org/10.1086/501424)
- Pe'er, A., & Waxman, E. 2004, *ApJ*, 613, 448, doi: [10.1086/422989](https://doi.org/10.1086/422989)
- Pe'er, A., & Zhang, B. 2024, arXiv e-prints, arXiv:2407.16241, doi: [10.48550/arXiv.2407.16241](https://doi.org/10.48550/arXiv.2407.16241)
- Piran, T. 1999, *PhR*, 314, 575, doi: [10.1016/S0370-1573\(98\)00127-6](https://doi.org/10.1016/S0370-1573(98)00127-6)
- Pozdnyakov, L. A., Sobol, I. M., & Syunyaev, R. A. 1983, *Astrophys. Space Phys. Res.*, 2, 189
- Ramaty, R., & Meszaros, P. 1981, *ApJ*, 250, 384, doi: [10.1086/159386](https://doi.org/10.1086/159386)
- Ravasio, M. E., Salafia, O. S., Oganesyan, G., et al. 2024, *Science*, 385, 452, doi: [10.1126/science.adj3638](https://doi.org/10.1126/science.adj3638)
- Roberts, O. J., Veres, P., Baring, M. G., et al. 2021, *Nature*, 589, 207, doi: [10.1038/s41586-020-03077-8](https://doi.org/10.1038/s41586-020-03077-8)
- Rybicki, G. B., & Lightman, A. P. 1979, Radiative processes in astrophysics (John Wiley & Sons)
- Shemi, A., & Piran, T. 1990, *ApJL*, 365, L55, doi: [10.1086/185887](https://doi.org/10.1086/185887)
- Shimoda, J., & Wada, T. 2025, *ApJ*, 986, 213, doi: [10.3847/1538-4357/add33c](https://doi.org/10.3847/1538-4357/add33c)
- Thompson, C., & Duncan, R. C. 1995, *MNRAS*, 275, 255, doi: [10.1093/mnras/275.2.255](https://doi.org/10.1093/mnras/275.2.255)
- . 2001, *ApJ*, 561, 980, doi: [10.1086/323256](https://doi.org/10.1086/323256)
- Veres, P., Fraija, N., Lesage, S., et al. 2024, arXiv e-prints, arXiv:2408.16748, doi: [10.48550/arXiv.2408.16748](https://doi.org/10.48550/arXiv.2408.16748)
- Wada, T. 2025, *PhRvD*, 112, 123027, doi: [10.1103/k3hz-k6v4](https://doi.org/10.1103/k3hz-k6v4)
- Wada, T., & Asano, K. 2025, *Progress of Theoretical and Experimental Physics*, 2025, 033E01, doi: [10.1093/ptep/ptaf033](https://doi.org/10.1093/ptep/ptaf033)
- Wada, T., & Ioka, K. 2023, *MNRAS*, 519, 4094, doi: [10.1093/mnras/stac3681](https://doi.org/10.1093/mnras/stac3681)
- Wada, T., & Shimoda, J. 2024, *ApJ*, 972, 58, doi: [10.3847/1538-4357/ad6847](https://doi.org/10.3847/1538-4357/ad6847)
- Wei, Y.-J., Ren, J., He, H.-N., et al. 2024, *ApJL*, 968, L5, doi: [10.3847/2041-8213/ad4ce1](https://doi.org/10.3847/2041-8213/ad4ce1)
- Yamasaki, S., Lyubarsky, Y., Granot, J., & Gögiş, E. 2020, *MNRAS*, 498, 484, doi: [10.1093/mnras/staa2223](https://doi.org/10.1093/mnras/staa2223)
- Yang, Y.-P., & Zhang, B. 2021, *ApJ*, 919, 89, doi: [10.3847/1538-4357/ac14b5](https://doi.org/10.3847/1538-4357/ac14b5)
- Yi, S.-X., Zhang, Z., Seyit Yorgancioglu, E., et al. 2024, arXiv e-prints, arXiv:2409.08485, doi: [10.48550/arXiv.2409.08485](https://doi.org/10.48550/arXiv.2409.08485)
- Zhang, B. 2018, *The Physics of Gamma-Ray Bursts* (Cambridge University Press), doi: [10.1017/9781139226530](https://doi.org/10.1017/9781139226530)
- Zhang, B. T., Murase, K., Ioka, K., & Zhang, B. 2025, *Journal of High Energy Astrophysics*, 45, 392, doi: [10.1016/j.jheap.2025.01.007](https://doi.org/10.1016/j.jheap.2025.01.007)
- Zhang, Y.-Q., Xiong, S.-L., Mao, J.-R., et al. 2024a, *Science China Physics, Mechanics, and Astronomy*, 67, 289511, doi: [10.1007/s11433-023-2381-0](https://doi.org/10.1007/s11433-023-2381-0)
- Zhang, Z., Lin, H., Li, Z., et al. 2024b, *ApJL*, 973, L17, doi: [10.3847/2041-8213/ad758e](https://doi.org/10.3847/2041-8213/ad758e)
- Zhu, J., Feng, H., & Liu, T. 2025, *ApJL*, 983, L33, doi: [10.3847/2041-8213/adc73a](https://doi.org/10.3847/2041-8213/adc73a)